Nanoscale

PAPER

View Article Online
View Journal | View Issue

Cite this: *Nanoscale*, 2016, **8**, 17581

Switch on the high thermal conductivity of graphene paper

Yangsu Xie,[a] Pengyu Yuan,[a] Tianyu Wang,[a] Nastaran Hashemi[a] and Xinwei Wang*[a,b]

Received 12th August 2016,
Accepted 9th September 2016

DOI: 10.1039/c6nr06402g

www.rsc.org/nanoscale

This work reports on the discovery of a high thermal conductivity (κ) switch-on phenomenon in high purity graphene paper (GP) when its temperature is reduced from room temperature down to 10 K. The κ after switch-on (1732 to 3013 W m^{-1} K^{-1}) is 4–8 times that before switch-on. The triggering temperature is 245–260 K. The switch-on behavior is attributed to the thermal expansion mismatch between pure graphene flakes and impurity-embedded flakes. This is confirmed by the switch behavior of the temperature coefficient of resistance. Before switch-on, the interactions between pure graphene flakes and surrounding impurity-embedded flakes efficiently suppress phonon transport in GP. After switch-on, the structure separation frees the pure graphene flakes from the impurity-embedded neighbors, leading to a several-fold κ increase. The measured κ before and after switch-on is consistent with the literature reported κ values of supported and suspended graphene. By conducting comparison studies with pyrolytic graphite, graphene oxide paper and partly reduced graphene paper, the whole physical picture is illustrated clearly. The thermal expansion induced switch-on is feasible only for high purity GP materials. This finding points out a novel way to switch on/off the thermal conductivity of graphene paper based on substrate-phonon scattering.

1. Introduction

The thermal conductivity (κ) of suspended and supported graphene has been investigated extensively. Due to the strong bonding among light carbon atoms, the phonon-dominated thermal conductivity of graphene is extremely high. For suspended graphene, a large thermal conductivity (κ) from 1500 to 5000 W m^{-1} K^{-1} was obtained experimentally at near room temperature (RT).[1–7] For the supported graphene, however, κ is reduced to a much lower level resulting from the phonons leaking across the graphene–support interface and strong interface scattering of flexural modes.[8] Cai *et al.* obtained the κ of single layered graphene (SLG) grown by chemical vapor deposition. For suspended graphene, κ exceeded (2500 + 1100/−1050) W m^{-1} K^{-1} at near 350 K and (1400 + 500/−480) W m^{-1} K^{-1} at about 500 K. When graphene was supported on Au-coated SiN_x, κ was determined to be (370 + 650/−320) W m^{-1} K^{-1} at RT, which is considerably lower due to the substrate effect.[4] Seol *et al.* investigated the κ of mono-layered graphene supported on silicon dioxide. The κ was measured to be about 600 W m^{-1} K^{-1} near RT,[8] which is 60%–88% lower compared to the κ of suspended graphene. Jang *et al.* measured the κ of graphene and ultrathin graphite encased within silicon dioxide to be lower than 160 W m^{-1} K^{-1} at 310 K.[9] The top layer oxide deposition resulted in an extra 64% and 38% reduction in the κ of three-layered and four-layered graphene flakes compared to the supported samples. Pettes *et al.* studied the influence of a polymeric residue on the κ of bilayer graphene. The κ was about 600 W m^{-1} K^{-1} and presented a $T^{1.5}$ behavior from 50 to 125 K.[10] Therefore, the substrate or impurity deposition makes a great difference to the κ of graphene. If the substrate effect is controllable, a thermal switch using graphene will be feasible. At a predetermined temperature, heat will transfer at an extremely high rate from a heat source to a heat sink.

The main heat carriers in graphene at near RT are acoustic phonons. When the temperature of a supported-graphene changes, phonon frequencies and phonon dispersion change, which contributes to the thermal property variation with temperature. Another important factor that impacts the thermal properties of supported graphene is the thermal strain induced by the thermal expansion mismatch between the substrate and graphene. Kuang *et al.* investigated the effect of tensile strain on the enhancement of the intrinsic κ of multi-layered graphene. From their calculation, the increasing tensile strain leads to a decreased heat capacity and increased lifetime of flexural phonons, which could enhance the intrinsic κ for multi-layered graphene.[11] Yoon *et al.* reported that the

[a]*Department of Mechanical Engineering, 2025 Black Engineering Building, Iowa State University, Ames, IA 50011, USA. E-mail: xwang3@iastate.edu; Tel: +1-515-294-8023*
[b]*School of Environmental and Municipal Engineering, Qingdao Technological University, Qingdao 266033, Shandong Province, P. R. China*

strain caused by the thermal expansion coefficient (TEC) mismatch between graphene and the substrate has a crucial role in determining the physical properties of graphene. From their Raman spectroscopy study, when the temperature was decreased to about 200 K, the thermal stress exceeds the van der Waals (VdW) force. The single layered graphene (SLG) on a SiO_2 substrate buckled, forming wrinkles or bubbles due to compressive strain.[12] Li *et al.* demonstrated that graphene flakes deposited on graphite can be sufficiently decoupled from the graphite substrate due to ridge-like defects, so as to exhibit the structural and electronic properties expected of pristine graphene.[13] As a summary, the strain in supported graphene could cause the graphene to decouple from the substrate and subsequently free the graphene from substrate phonon scattering. Under this circumstance, the graphene flake is expected to present thermal and electrical properties similar to that of suspended pristine graphene.

Large area freestanding graphene paper (GP) has been extensively studied in order to utilize the excellent properties of graphene in industry. GP is a bulk material with anisotropic thermal transport capability. Although the thermal transport is expected to be limited by the abundant pore structure and small flake size, the reported κ ($\geq$1000 W m^{-1} K^{-1} at RT)[14] and electrical conductivity ($\sim 1.57 \times 10^5$ S m^{-1})[15] of GP is much higher than those of other graphene-based bulk materials. These results indicate that the boundary scattering in GP does not strongly impact the phonon propagation in GP. Potential applications of GP in high performance electrode materials,[16] as a good gas barrier,[17] biocompatible material, in Li ion battery anodes,[18–20] and energy storage devices[21,22] have been reported. Among the various developed methods for fabricating GP, including chemical reduction, acid intercalation followed by thermal exfoliation, heating graphene oxide paper in different environments, *etc.*,[23–26] heating graphene oxide films in an ultra-high vacuum was reported to be particularly effective.[27] Recently Xin *et al.* reported the fabrication of a highly ordered graphene paper by using direct electro-spray deposition of graphene films integrated with a continuous roll-to-roll process.[15] Subsequent thermal annealing was applied to remove functional groups and structural defects. It was reported that 2200 °C is the optimized temperature for thermal annealing, after which the thermal and electrical conductivities could reach 1238.3 W m^{-1} K^{-1} and 1.57×10^5 S m^{-1} respectively at RT.[15] Song *et al.* investigated the structural evolution of the thermally reduced graphene oxide film (r-GO), and correlated the different annealing temperatures with the κ and mechanical performances of r-GO. When the temperature reached 1200 °C, the r-GOF had an ultrahigh κ of 1043.5 W m^{-1} K^{-1}. 1000 °C was found to be a critical temperature in enhancing κ.[14]

To have a better understanding of the thermal performance of GP at low temperatures and study the phonon scattering mechanisms in such structures, we intend to study the thermal reffusivity (reciprocal of thermal diffusivity) of GP. Thermal reffusivity (Θ) is first defined and used to characterize the phonon thermal resistivity.[28] It is an intrinsic property of materials which solely depends on the phonon propagation in the materials. In our previous work, it was found that as the temperature goes down, Θ decreases and finally reaches a stable residual value at the 0 K limit.[28–31] The residual thermal reffusivity (Θ_0) at very low temperatures can be used to characterize the in-plane domain size and to quantitatively estimate the defect level of materials. The higher the Θ_0, the more are the defects and impurities found in the materials.[30] In our previous work, the thermal reffusivity model was developed in detail and used to quantitatively analyze the defect level of different materials, including graphene foam and pyrolytic graphite.[30] By fitting the experimental data with the thermal reffusivity model, phonon scattering intensities at different temperatures were revealed. It was demonstrated that the thermal reffusivity model can provide sound estimation of the Debye temperature and structure domain size of graphene foam and pyrolytic graphite.[30]

For the highly reduced (~99% carbon) and ordered GP material, we found a very interesting phenomenon: as the temperature decreases from RT (295 K) to about 245 K, there is a sudden jump of κ from ~500 W m^{-1} K^{-1} to ~2000 W m^{-1} K^{-1}. For comparison, the κ of graphene oxide paper (GOP) and partly reduced graphene paper (PRGP) samples are also measured. The result indicates that κ switch-on only occurs in highly reduced and ordered GP. To better understand the physical mechanisms for the κ switch-on in GP, we characterize the unique morphology and chemical structure, temperature coefficient of resistance (TCR), and thermal diffusivity profile. Using the thermal reffusivity model, the Debye temperature and average domain size of GP are determined. The structure and thermal reffusivity of GOP and PRGP are further studied and reported. By conducting a comparison study with pyrolytic graphite, GOP and PRGP, and analyzing the different phonon scattering behaviors, the whole physical picture for κ switch-on in GP is illustrated clearly.

2. Graphene paper structure

The graphene paper material was purchased from a graphene supermarket and used as received. Fig. 1 shows the morphology and structural characterization of the GP material. Fig. 1(a) and (b) show the image of GP under a scanning electron microscope (SEM) with 500× magnification. The GP presents a grey color under SEM. The top layer shows a seamless surface with small ridges. From Fig. 1(b), the stacking layered structure can be seen clearly. The top layer can be peeled off, which demonstrates the strong planar and weak interlayer bonding force. The inset in Fig. 1(a) presents a contact mode atomic-force microscopy (AFM) topology image (MicroNano AFM 3000) of GP. The average height variation of the surface along the blue line shown in the 0.6 × 0.6 μm scanning area is about 0.23 nm, which illustrates the high smoothness of GP. The inset in Fig. 1(b) is a digital optical microscope image of GP. As shown in the inset, the GP is grey with a metallic luster, which is the typical color of a high purity graphene

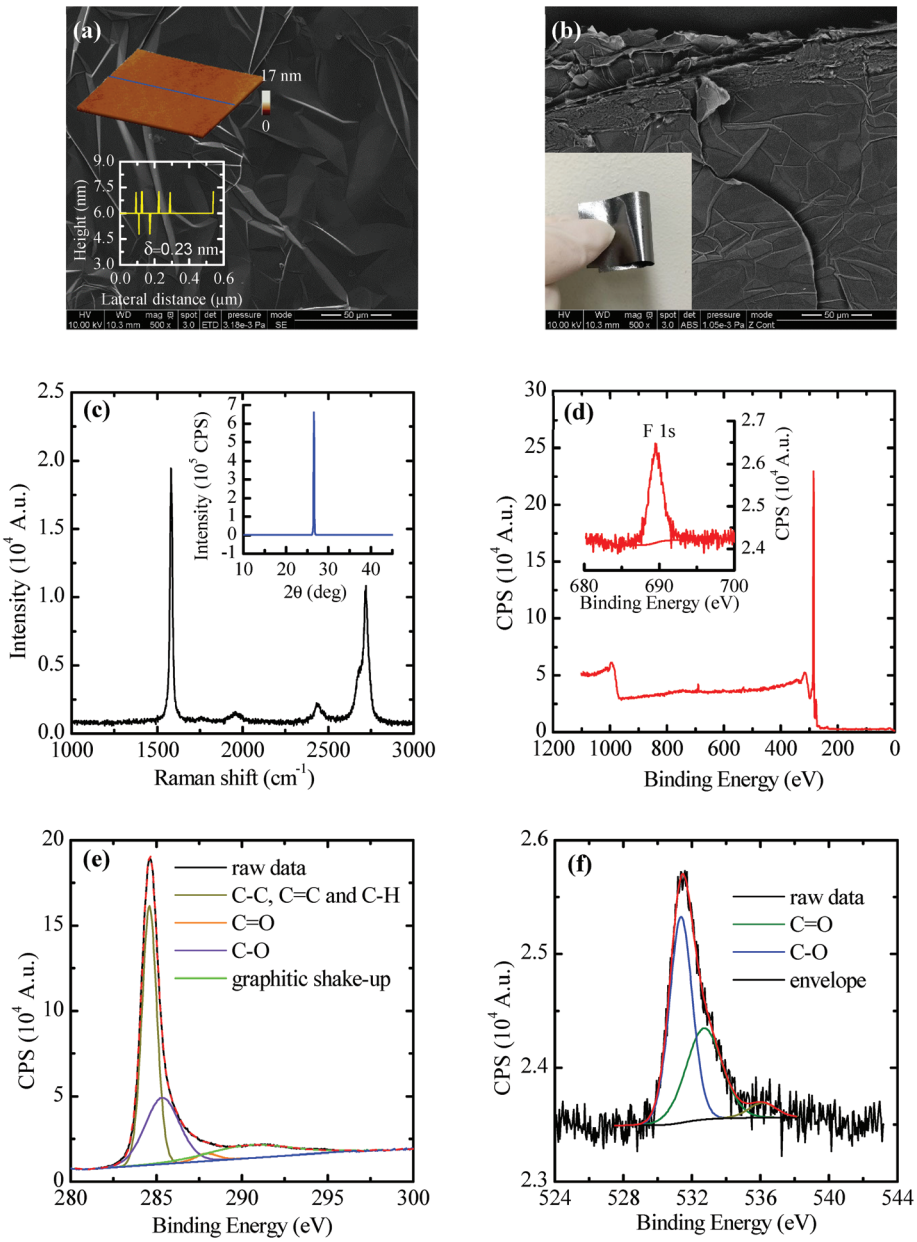

Fig. 1 Morphology and structure characterization of the GP sample. (a) and (b) SEM images of the GP under 500× magnification. The inset in (a) shows an AFM topology image. δ = 0.23 nm is the average height variation of the surface along the blue line. The layered stacking structure of GP can be seen clearly in (b). The inset in (b) shows the flexibility of the GP. (c) The Raman spectrum. The inset shows the XRD spectrum. (d) X-ray photoelectron spectra. The inset shows the XPS F 1s spectrum, suggesting the presence of fluorine. (e) The XPS C 1s spectrum, indicating different bonds for carbon atoms in the GP sample. (f) The XPS O 1s spectrum, suggesting the residual oxygen-containing functional groups.

material.[14] The GP is very flexible and can be easily bent and recovered.

The Raman spectra of GP shown in Fig. 1(c) exhibit two pronounced peaks at 1581 and 2719 cm^{-1}, corresponding to the G peak and 2D peak. The D peak is invisible while the G peak is very sharp, which indicates the rare defects and the high crystallinity of a graphene sheet. In order to identify the number of layers in the graphene sheet, Raman spectra are obtained at 30 different locations on a GP sample. By integrating the G peak and 2D peak, the ratio of the intensity of the G peak to the 2D peak is estimated to be 0.61–0.72, which corresponds to 5–6 layers of graphene.[32] For comparison, the I_G/I_{2D} of highly oriented pyrolytic graphite (HOPG) is about 0.85.[32] The inset in Fig. 1(c) presents the X-ray diffraction pattern (XRD, Siemens D500 X-ray diffractometer using a Cu X-ray tube) of GP. The sharp and distinct peak around 26.6 degrees 2θ corresponds to the (002) plane, from which the interlayer spacing of GP is determined to be 3.35 Å. For pristine natural graphite, the interlayer distance is also 3.35 Å.[33] This result demonstrates that the GP has high purity and an excellent ordered

structure. The amount of functional groups or other structural impurities is very small.

To further characterize the chemical composition of GP, an X-ray photoelectron spectrometer study (XPS) is conducted. Fig. 1(d) presents the XPS survey spectrum of the GP. The resulting elemental composition of the GP is C 1s (98.91%), O 1s (0.66%), and F 1s (0.43%), which indicates that the GP is composed of highly purified graphene films. The inset in Fig. 1(d) shows the narrow scan spectrum of F 1s. A prominent peak at 689.5 eV indicates the presence of the C–F bond on the surface of the GP.[34] Fig. 1(e) is the narrow scan spectra of C 1s. The C 1s spectra main peak can be deconvoluted into mainly four components: C–C at 284.6 eV, C–O at 285.4 eV, C═O at 287.9 eV and π–π* transition at 290.5 eV.[35,36] The C–C peak is dominant in the C 1s main peak. Fig. 1(f) shows the deconvoluted narrow scan of O 1s. Two peaks can be fitted into C–O at 531.4 eV and C═O at 532.7 eV. The above analysis concludes that the GP is highly carbonized graphene with a very small amount of oxygen (0.66%) and fluorine (0.43%) containing functional groups. The F amount in GP is very small. From literature reviews about the synthesis process of GP,[14,15] we feel that the residual trace of the F element originates from the graphene oxide material which is used for the synthesis of the final GP material.

3. Switch on by temperature reduction: analyzed using thermal diffusivity and reffusivity

The thermal diffusivity of GP is measured using the transient electrothermal (TET) technique. The experimental details can be found in the Experiment details section. Fig. 2(a) presents the schematic of the experimental set up, which shows the suspended sample placed on the stage of the cold head of a closed cycle refrigerator system. Two GP samples are measured in this work. Three rounds of experiments are conducted, denoted as S1_round1, S1_round2 and S2 respectively. The details of the two samples are summarized in Table 1.

3.1 Thermal diffusivity switch-on observation and physics

A. Observation of thermal diffusivity jump. Fig. 2(b) and (c) show the *V*–*t* raw data and the theoretical fitting of the TET measurement of S2 at six different temperatures: 295 K, 245 K, 220 K, 210 K, 195 K and 75 K. During the TET experiment, a current of 160–280 mA is used, so as to make sure that the voltage change due to joule heating takes only about 1.3% of the total voltage. The temperature increase of the sample is about 2.6 K at 10 K to about 23.5 K at 295 K. From 295 K to

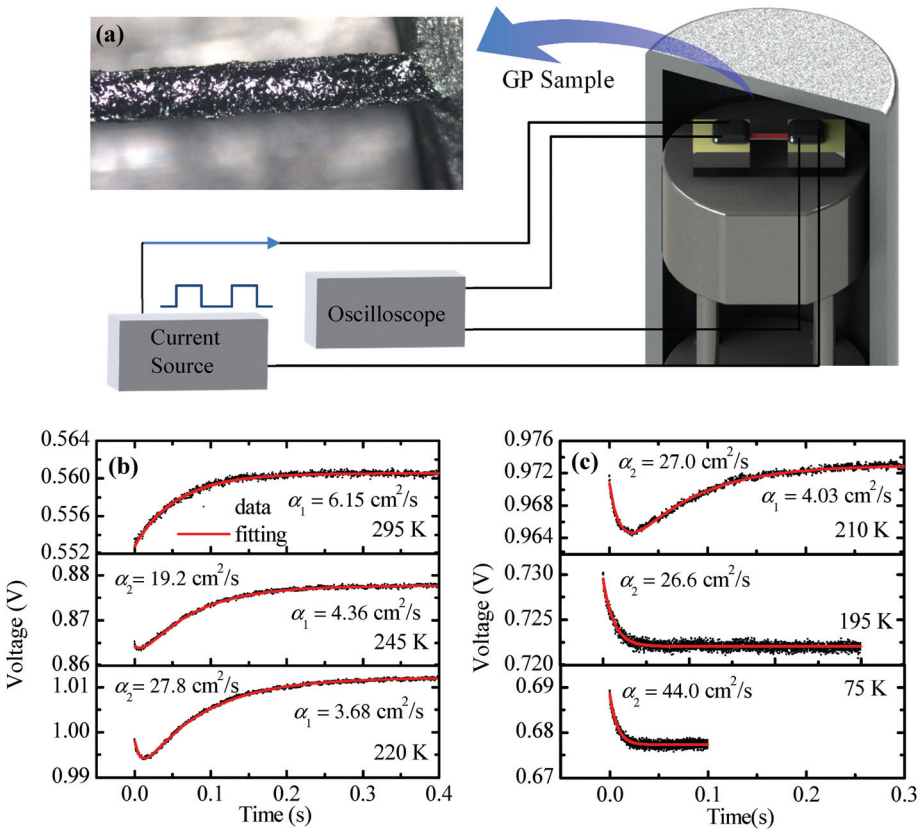

Fig. 2 (a) The schematic of four-probe TET experiment and sample set up in the cold jacket of the CCR system. Four-probe *I*–*V* measurement is employed in the experiment to avoid the influence of contact resistance. (b), (c) The evolution of voltage against time for S2 at different temperatures. As the temperature goes down, the profile transforms from a pure voltage increasing to pure voltage decreasing pattern.

Table 1 Details of the samples measured in this work

Sample type	Index	Length [mm]	Width [mm]	Thickness [μm]	Density [kg m^{-3}]
GP	S1	16.7 ± 0.1	0.28 ± 0.05	28.6 ± 1.0	1623 ± 66
GP	S2	18.5 ± 0.1	0.20 ± 0.03	28.6 ± 1.0	1623 ± 66
PRGP	S1	2.3 ± 0.06	1.1 ± 0.06	17.3 ± 2.5	1466 ± 212
PRGP	S2	1.3 ± 0.07	0.5 ± 0.01	17.3 ± 2.5	1466 ± 212
PRGP	S3	1.4 ± 0.05	0.2 ± 0.01	17.3 ± 2.5	1466 ± 212
GOP	NA	1.1 ± 0.01	0.2 ± 0.002	33.6 ± 2.1	1357 ± 117

195 K, the TET signals present a very interesting evolution. At RT, the voltage of the sample presents an increasing behavior with the joule heating and then becomes stable, which is a typical TET signal for materials with a positive TCR. As the temperature goes down to 245 K, a small decreasing part emerges at the beginning of the TET signal, after which the signal increases and becomes stable. From 245 K to 210 K, the decreasing part develops and begins to dominate the entire TET signal. As the temperature goes down to 195 K, the TET profile monotonically decreases and then reaches the steady state, which is similar to the TET signal of other graphene based materials.[30,37] These data indicate that from RT to low temperature, the TCR of GP changes from positive to negative. This TCR change will be elaborated by the R–T study below.

To fit the TET raw data, two different fitting models are used. The fittings for the monotonically increasing or decreasing TET signals are based on the theoretical model of eqn (1) in the Experimental details section and conducted with MATLAB programming.[38] When the increasing part and decreasing part are both observed, a new theoretical model is constructed to characterize the new phenomenon: $T^* = a[\exp(-9.911 \times \alpha_1 t/L^2)] + b[\exp(-9.911 \times \alpha_2 t/L^2)] + c$. In this model, α_1 and α_2 are two different thermal diffusivities corresponding to two simultaneous heat transport mechanisms in GP. The terms in the square brackets are the simplified form of eqn (1). Therefore, the new model assumes two simultaneous heat transport processes in GP and considers them to be independent. A linear relationship is used for summarizing the contribution of the two independent heat transports. The physical principle for the model is elaborated in the next section. From Fig. 2(b) and (c), the model gives excellent fitting for the V–T raw data. The resulting α_1 and α_2 values are also presented at each temperature. Different trial values of α are used for the fitting. The fitting error is determined to be ±10% or better, which has been studied carefully in our previous work on the TET technique.[39,40]

B. Thermal diffusivity switch-on: results. The measured thermal diffusivities of the three samples denoted as S1_round1, S1_round2 and S2 are presented in Fig. 3(a). Two separate data groups are observed for all the three samples. The lower thermal diffusivity group is denoted as α_1, and the higher thermal diffusivity group is denoted as α_2. As illustrated above, α_1 and α_2 are two different thermal diffusivities corresponding to two thermal transport states in GP samples. α_1 (3.68×10^{-4}–5.57×10^{-4} m^2 s^{-1}) is much lower than α_2 (1.92×10^{-3}–6.49×10^{-3} m^2 s^{-1}). Before switch-on, α_1 dominates the thermal transport in GP. As the temperature goes down, α_1 decreases slowly. The jumping of the thermal diffusivity from α_1 to α_2 starts at about 245–260 K for all the three samples. From 245 K to 195 K, there are two different thermal transport phenomena coexisting in GP, corresponding to α_1 and α_2 in the TET fitting model. The resulting α_1 and α_2 are both presented in the figure. At the same temperature point, α_2 is about 5–8 times higher than α_1. After switch-on, the TET signal is pure voltage decreasing. α_2 becomes a dominant thermal transport mechanism in GP. From 195 K to 10 K, α_2 increases with the temperature decreasing rapidly from 260 K to 75 K. Below 75 K, α_2 becomes relatively stable. The α_2–T profile is very similar to that of GF and graphite.[30] There is a drop in α_2 for S2 at 45 K to 10 K. It might be the result of a loose connection between S2 and the electrodes at very low temperatures. Since the sample's resistance is fairly small [as shown Fig. 3(b)], a small connection degradation will affect the results. In this section, our focus is on the ultra-high thermal diffusivity switch-on. The variation trend of thermal diffusivity against temperature will be analyzed and explained following the thermal reffusivity concept in the next section.

C. Mechanism of the thermal diffusivity jump. For the two thermal transport mechanisms, we ascribe α_1 to the graphene flakes subjected to substrate phonon scattering by neighboring flakes and α_2 to the suspended portion of graphene flakes. The jump of thermal diffusivity from α_1 to α_2 is due to the separation of the graphene flakes induced by temperature reduction and TEC mismatch. Fig. 3(c) shows the schematic of the structure separation in GP due to temperature reduction and thermal expansion mismatch. At high temperatures (295 K–245 K) where the graphene flakes are stacked with a small inter-flake distance, the graphene flakes can be regarded as supported graphene on a substrate of neighboring graphene flakes. From XPS analysis, GP consists of about 0.66% O and 0.43% F. Although these impurities account for a very small proportion of the chemical composition, they could provide a large scattering effect for phonons. The phonon propagation along the in-plane direction is largely impeded by the extra atoms. For the pure graphene flake domain, the neighboring flake scattering effect limits α_1 to a great extent by phonon–substrate interaction.[4,8,9]

The pure graphene flakes in GP present a negative thermal expansion coefficient at near RT according to the experiment and numerical calculations.[12] Huang *et al.* studied the disorder-induced thermal contraction in functionalized graphene. They found that the functionalization suppresses (enhances) the thermal contraction (expansion) of the lattice, due to the increase in the system mass, membrane thickness, and the compressibility of phonons.[41] GP in our work consists of about 0.66% O and 0.43% F. The impurity-embedded flakes in GP are expected to present a less negative or even positive thermal expansion coefficient. As the temperature goes down, the discrepancy of thermal expansion between pure graphene and impurity-embedded flakes results in biaxial tensile strain in impurity-embedded flakes and compressive strain in pure

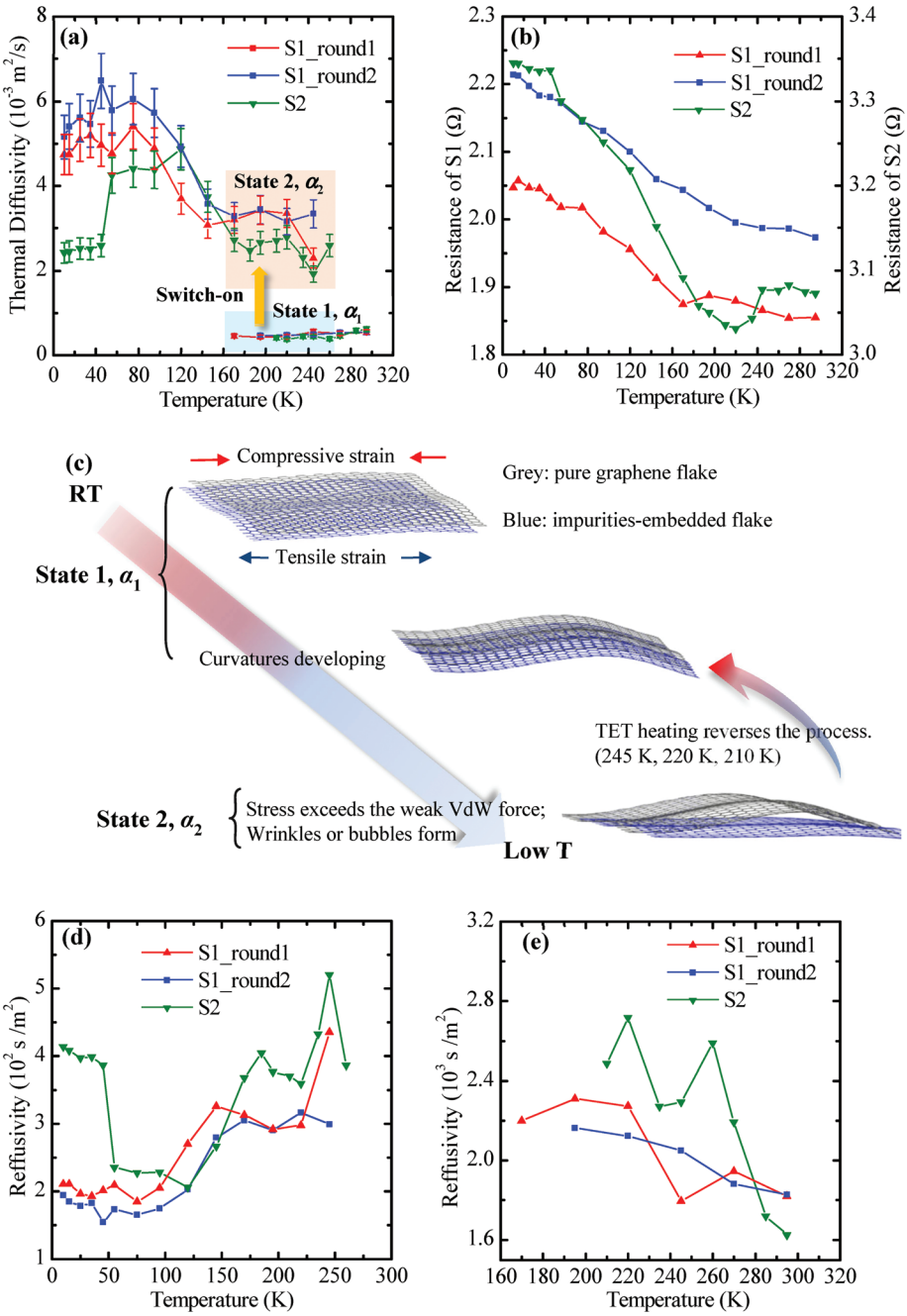

Fig. 3 (a) The thermal diffusivity of GP. (b) The resistance against the temperature profile of GP. (c) The schematic drawing illustrates the reversible structure separation process between pure graphene flakes (grey) and impurity-embedded flakes (blue) as the temperature goes down. (d) The thermal reffusivity of GP after switch-on. (e) The thermal reffusivity of GP before switch-on.

graphene flakes. Although the tensile strain in impurity-embedded flakes could improve the thermal transport a little as indicated in Kuang *et al.*'s work,[11] the compressive strain in pure graphene flakes reduces the κ as reported in literature studies.[42,43] Since the pure graphene flakes play a dominant role in the thermal transport of GP, the overall κ of GP presents a slowly decreasing pattern as the thermal strain is built up by a lowered temperature. The thermal strain builds up as the temperature goes down, but without structure separation. Although graphene itself has a negative TCR, the compressive strain in graphene will make its electrical resistance decrease against reduced temperature. This effect is stronger than the intrinsic TCR of graphene, leading to an overall positive TCR. The positive TCR of graphene under strain has been observed and studied in our previous work, in which the thermal strain due to the thermal expansion mismatch between graphene and the PMMA substrate resulted in a positive TCR of graphene. When the thermal expansion mismatch becomes

smaller at low temperatures, the effect of the intrinsic negative TCR of graphene becomes more significant. As a result, the TCR becomes less positive. When graphene and PMMA separate at low temperatures, the TCR goes back to negative.[44] The positive TCR of graphene on the substrate is also reported in other literature studies. Pang *et al.* reported an increasingly positive TCR of the polymer/graphene composite thermally treated at 180 °C.[45] Therefore, when the strain effect exceeds the intrinsic TCR effect, the TCR of graphene becomes positive. That is why we observed a resistance increase during TET heating, like that at 295 K. This type of overall positive TCR for supported graphene is also observed in our work for few-layered graphene supported on poly(methyl methacrylate) (PMMA) and studied in detail.[44] Therefore, in this state, the TET signal presents a pure voltage-increasing pattern. The thermal diffusivity is entitled α_1.

As the temperature goes down, curvatures first develop for the graphene flakes. When the temperature is further lowered down, the increasing thermal strain causes a significant TEC mismatch among pure graphene flakes and the impurity-embedded flakes. The two materials separate, as shown in Fig. 3(c). The thermal diffusivity of this state is α_2. In this state, since the graphene is strain free, strain-induced electrical resistance change disappears. As a result, the TCR of the sample is more controlled by the intrinsic TCR of graphene, which is negative. Therefore, a decrease of the electrical resistance is observed in TET heating, as is shown in the TET experiments at 195 K and 75 K in Fig. 2(c). This kind of high temperature positive TCR transfer to negative TCR at reduced temperatures was also observed for PMMA-supported graphene, and has been explained in detail in our work.[44] The thermal diffusivity of this state α_2 is expected to be much higher than α_1 since the graphene flake is not or much less subjected to substrate phonon scattering.

D. Physics behind the two-style *V*–*t* curve in TET. For the two-style *V*–*t* curve (first decreasing, then increasing) in the TET experiments at 245 K, 220 K, and 210 K, they can be explained as below. At 245 K, since this temperature is not very low, although the graphene flake separates from the neighboring substrate, this separation is not on a large-scale. The free standing part in graphene flakes still plays a dominant role in phonon propagation at the beginning of thermal transport. Thus, at the beginning of the TET heating, the sample shows a negative TCR, as observed in the figure for voltage decrease. But after the sample has been heated up by the electrical current a little bit, its temperature goes up. Subsequently, the graphene flakes thermally contract, which reverses the already existing structure separation. As a result, the graphene flakes are in contact with the impurity-embedded flakes again. The overall sample's TCR becomes positive again and its thermal diffusivity goes down. This is the reason why we do the TET two-step heat transfer, the voltage decreasing part gives a very high thermal diffusivity (α_2), which represents the state of graphene separated from the neighboring flakes. The voltage increasing part gives a lower thermal diffusivity (α_1), which represents the state in which the graphene flakes are in sound contact with the neighboring flakes. When the temperature is reduced further from 245 K, as presented at 220 K, it requires more heating in TET to reverse the structure separation state. Thus, an increased contribution of the voltage decreasing part is observed from 245 K to 220 K. This part makes more contribution in the case of 210 K. When the temperature is reduced more, the voltage decreasing part dominates all the heat transfer processes. As the pure graphene flakes are completely separated from the impurity-embedded graphene flakes, the structure-separation cannot be reversed any more during the TET heating cycle. From 195 K to 10 K, the phonon scattering intensity decreases with the decreasing temperature, which is controlled by the phonon population and interface scattering.

Our above analysis is also backed up by the observation of the electrical resistance change against temperature. Fig. 3(b) shows R_0 (electrical resistance before TET heating) against environmental temperature T_0. In the region close to RT, although not obvious, R decreases with decreased T slowly. The built-up compressive strain in the graphene flakes induced by temperature reduction decreases its electrical resistance. When the temperature is reduced more, this trend changes to a completely negative TCR relationship. Also this TCR is quite constant, featuring an almost linear *R*–*T* relationship, which is very similar to the graphene foam we studied before.[30] The *R*–*T* curve is also in accordance with the dominating role shifting from α_1 to α_2 at certain temperatures. GP has an extremely high electrical conductivity of about 4.4×10^4 S m^{-1} at RT. For S2, an evident valley value is observed at around 220 K. From 295 K to 220 K, R_0 drops from 3.07 Ω to 3.043 Ω; from 220 K to 10 K, R_0 begins to increase as T_0 goes down. The R_0–T_0 behavior agrees with the increasing and decreasing parts of the TET profiles respectively. For S1_round1 and S1_round2, although the *V*–*T* signals in the TET experiment present a positive-to-negative TCR changing behavior, the TCR of R_0 does not show any evident valley value. Instead, a changing slope of R_0 occurs at 170 K for S1_round1 and at 220 K for S1_round2. Both these changing points are in accordance with the switch-on temperature of thermal diffusivity for the two rounds of S1. The reason why the valley value is not evident is attributed to the base heating/cooling effect. During TET signal collection, only the GP sample is heated and the base is kept at a constant temperature. However, the R_0–*T* profile is obtained by changing the temperature of the whole environment including the sample base. Under this situation, the electrical contact resistance between GP and electrodes could be affected by the changing temperature, which also contributes to the R_0 profile. Since the resistance of GP is very small, even a small contact resistance variation could have a large influence over the resistance change. In addition, S1 has a relatively higher thermal diffusivity than that of S2 for the whole temperature range. This indicates that S2 might contain a higher density of impurities than that of S1. The triggering temperature of S2 is higher than that of S1. This implies that at the same temperature, S2 is endowed with higher thermal stress which exceeds the VdW force among the flakes and facilitates the flakes' separation. Under this situ-

ation, the thermal strain effect on the resistance of S2 is more evident than that of S1, which results in a clear valley value near the triggering temperature.

3.2 Structure evolution revealed by thermal reffusivity

We intend to use the thermal reffusivity theory to study the structure of the GP and compare it with that of graphene foam and graphite which we reported in our previous work.[30]

Fig. 3(d) shows the Θ of GP after ultra-high thermal transport switch-on. Since the error bars for α are already given in Fig. 3(a), the error bars for Θ are omitted for clarity. Θ decreases as the temperature goes down. As the temperature decreases to 95 K, the Θ of the three GP samples becomes stable at around 200 s m^{-2}. For S2, there is a sudden jump of the data at 45 K. It could have resulted from the electrode connection of the sample being loose at very low temperatures. Evidently, the pattern of Θ for GP after switch-on is similar to that of graphene foam, graphite and most of the crystallite materials.[28,30] In our previous work, it was found that for most materials, the Θ decreases with decreased temperature and finally reaches a stable residual value, just like the normal electrical resistivity behavior of metals. It is well-known that ZA phonons with a smaller wavenumber are far more prevalent in the thermal transport of graphene. Therefore, the normal scattering (N-scattering) of the ZA phonon is strong compared to the Umklapp scattering.[46,47] At near RT, the N-scattering dominates the phonon scattering for mono-layered graphene, multi-layered graphene and graphite of μm size especially at low temperatures (10 K–300 K). As the temperature goes down, lattice elastic vibrations weaken and the phonon population drops. The intensity of the N-scattering decreases subsequently, which results in the decreasing thermal reffusivity. At low temperatures, the N-scattering finally diminishes to a negligible level. The residual thermal reffusivity (Θ_0) is determined by the impurities and the defect scattering in the sample.

The three groups of experimental data are fitted using the thermal reffusivity model, which is expressed as $\Theta = \Theta_0 + C \times \exp(-\theta/2T)$.[30] In this model, Θ_0 is induced by the boundary and defect scattering of phonon, and it is assumed to be independent of the temperature. θ is the Debye temperature, and C is a constant parameter. By fitting with OriginPro, the resulting Θ_0 is 195 ± 20 s m^{-2} by averaging the three GP samples. Using the phonon velocity of 9171 m s^{-1}, the in-plane structure domain size of GP is estimated to be $l_{grain} = 3(v \times \Theta_0) =$ 1.68 μm.[25] The Debye temperature of GP is determined to be 610 ± 233 K. Many studies calculated high Debye temperature values for graphene, which are above 1000–2000 K.[27,48,49] For the three acoustic modes in graphene, the corresponding Debye temperature is 2840 K for the longitudinal mode (LA), 1775 K for the transverse mode (TA) and 1120 K for the flexural acoustic (ZA).[50] Theoretical calculations suggested that the ZA phonon dominates the thermal transport in graphene.[8,50,51] For few-layered graphene, the out-of-plane acoustic phonons still dominate the thermal conductivity.[52] From our previous work, the calculated Debye temperature for pyrolytic graphite is very close to that of the ZA mode. In this work, the Debye temperature of GP calculated from the thermal reffusivity model is much lower than the literature values. This discrepancy could be attributed to the structure change of GP at low temperatures. From our thermal reffusivity model, one assumption is that the phonon scattering intensity due to impurities and boundaries is independent of temperature. Only under this circumstance, Θ_0 can be considered as a constant. However, GP experiences thermal expansion among flakes which distorts the shape and size of the contacting area. The change in the inner structure of GP with temperature results in a large increase of the boundary scattering intensity. As a consequence, Θ_0 is overestimated. The higher Θ_0 leads to significant underestimation of θ from the model. Therefore, our estimate should be taken as a lower bound of the magnitude of the Debye temperature.

Before ultra-high thermal transport switch-on, the Θ of GP decreases slowly with temperature [see Fig. 3(e)], which is completely different from the trend of graphite. This phenomenon illustrates that the thermal expansion and lattice strain among the graphene flakes has a major influence on the thermal transport near RT (295 K–170 K). Thermal expansion contributes to thermal resistance, particularly at high temperatures.[53] The compressive thermal strain degrades the thermal contact among graphene flakes. As a result, the phonon scattering intensity increases as the temperature goes down before switch-on.

4. Thermal conductivity: switch-on

Using the specific heat of graphite and the density of the GP, the thermal conductivity of GP is calculated. Although the structures of GP and graphite are different, the difference in the specific heat between them is expected to be small. GP is made of high purity graphene. There are no experimental data on the specific heat of graphene to the best of our knowledge. From the literature, the low-temperature specific heat of graphene is expected to be a little higher than that of graphite due to the contribution of low-frequency ZA phonons. Above 100 K, graphene has an identical specific heat as that of the graphite.[54] The computer modeling results of the specific heat of graphene are presented in Fig. 4(a). The interlayer spacing of GP is similar to that of graphite (3.35 Å). The deviation resulted from ZA mode phonons in 5–6 layers graphene in GP is expected to be smaller than that of single layered graphene.[55] The specific heat of GP should be similar to that of graphite. Therefore, it is physically reasonable to use the experimental data of graphite as the specific heat of GP. The experimental data of the specific heat of graphite[56] and the numerical calculation result of SLG are plotted in Fig. 4(a) for comparison purposes. The density measurement is conducted by measuring the weight and volume of a GP sample. Using an analytical balance (Radwag xA 82/220/2X), the weight of the to-be-measured GP sample is 120.92 ± 0.04 mg. The sample dimensions are 5.02 cm × 5.19 cm × 28.6 μm. The thickness of

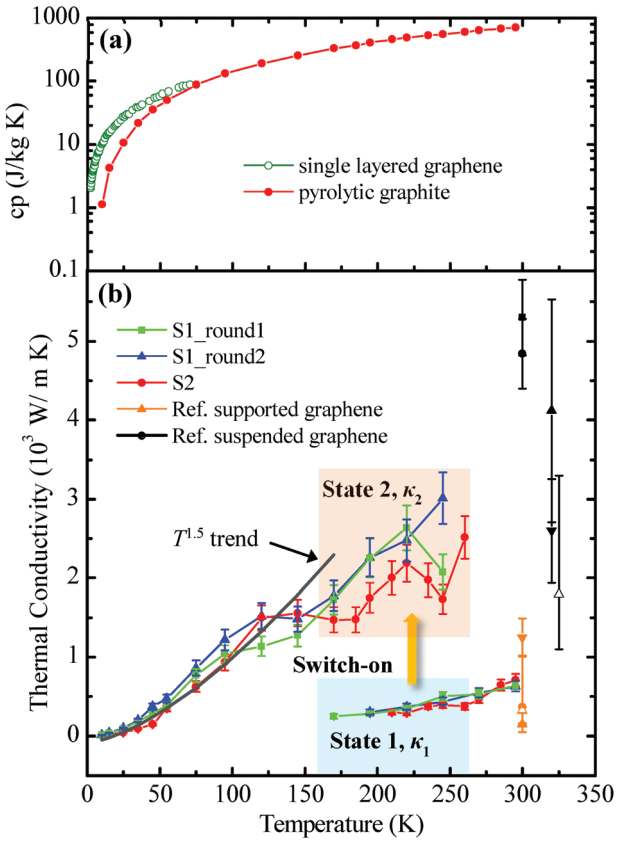

Fig. 4 (a) The experimental specific heat data of graphite and the calculated specific heat data of single-layered graphene from the literature for comparison.[54] This experimental data of graphite is used for calculating the thermal conductivity of GP. (b) The switch-on of the thermal conductivity of two GP samples. At low temperatures, κ presents a $T^{1.5}$ trend as shown by the solid black line in the figure. The literature reported thermal conductivity of graphene is presented in the figure to help the readers better understand the level of our thermal conductivity. The thermal conductivity of our GP should be lower than that of graphene due to the intrinsic structure phonon scattering. The black solid circles, solid square and hollow triangle are the literature reported κ for suspended mechanically exfoliated mono-layered graphene.[7,59] The black solid upward triangle and downward triangle are the literature reported κ of suspended isotopically pure ^{12}C (0.01% ^{13}C) graphene and 99.2% ^{13}C graphene respectively.[7] The orange solid circle presents the reported κ of supported mono-layered graphene.[4,58] The orange triangles are the κ of supported three-layered graphene.[50]

the sample is measured using a screw thread micrometer. The measured volume is 74.51 ± 2.51 mm^3. Thus, the density of GP is determined to be 1623 ± 55 kg m^{-3}.

Fig. 4(b) shows the measured thermal conductivity of GP. The κ of the three samples present similar values and patterns. In the temperature range of about 260 K to 170 K, an evident jump of κ from about 500 W m^{-1} K^{-1} to about 2200 W m^{-1} K^{-1} is observed. From RT to the triggering temperature, κ of the three data groups are slowly decreasing from 634 W m^{-1} K^{-1} to 246 W m^{-1} K^{-1}. For S1_round1 and S1_round2, the switch-on of κ starts at 245 K and completes at 170 K and 195 K respectively. For S2, the switch-on occurs at 260 K–210 K. Upon switch-on, κ becomes 4.13–7.95 times the κ before switch-on at the same temperature. As the temperature continues to goes down, κ of the three samples exhibits a rapid reduction. At very low temperatures (45 K–10 K), κ continues to decrease with a reduced rate from 148–372 W m^{-1} K^{-1} at 45 K to 4.4–9.4 W m^{-1} K^{-1} at 10 K. From 10 K to 95 K, κ follows a power temperature trend of $T^{1.5}$, as shown in Fig. 4(b). This indicates that the dominating phonon scattering in GP becomes defect and boundary scattering.[57] To check if the switch-on is a reversible process or not, S1_round2 is conducted as a repeated experiment of S1_round1 using the same sample. From Fig. 4(b), the result of round2 mostly coincides with that of round1, which indicates that the switch-on of GP is reversible. The switch-on does not change the structure of GP permanently. When the temperature is increased back to RT, the separation among the graphene flakes disappears and the structure returns to the original contacting state. When the temperature goes down to 245 K, the mismatch and separation among graphene flakes emerge again. As a result, κ jumps from 529 W m^{-1} K^{-1} at 270 K to 3013 W m^{-1} K^{-1} at 245 K again. The ending temperature of the switch-on process for round2 (195 K) is a little higher than that of round1 (170 K). It could result from the fact that the preceding separation process makes it easier for the separation of the graphene flakes during the second round experiment.

Before switch-on, κ is measured to be 634–710 W m^{-1} K^{-1} at RT, which is comparable with the literature reported κ of supported graphene. The κ of 150–1250 W m^{-1} K^{-1} was reported for three-layered graphene with different lateral dimensions supported on a SiN_x substrate.[58] Seol *et al.* reported the RT thermal conductivity of mono-layered graphene supported on silicon dioxide to be 600 W m^{-1} K^{-1}.[8] Cai *et al.* obtained the κ for Au/SiN_x membrane supported mono-layered graphene to be (370 + 650/−320) W m^{-1} K^{-1} at RT.[4] Our κ near RT is similar to the reported values of supported graphene at RT, which demonstrates that the thermal transport in GP before switch-on is largely suppressed by contacting with neighboring impurity-embedded graphene flakes. After switch-on, the graphene flakes are free from the neighboring phonon scattering. Under these circumstances, the structure of GP can be regarded as being interwoven with suspended graphene flakes. The resulting κ is expected to be comparable with the high κ value of suspended graphene.[13] From Fig. 4(b) it is seen that the thermal behavior of graphene flakes in GP after switch-on is similar to that of reported suspended graphene. For GP, the κ of the three samples at 245 K ranges from 1732 to 3013 W m^{-1} K^{-1}. From the literature, the κ of single-layered suspended graphene is reported to be about 1800–5000 W m^{-1} K^{-1} at RT.[59] For comparison, the κ of graphite is about 1781–1960 W m^{-1} K^{-1} from literature reports.[60–62] After switch-on, GP has a very high κ similar to that of graphite and smaller than that of the suspended single-layered graphene. This is reasonable considering that the GP is composed of about 5–6 layers of graphene flakes. It has been reported that as the number of layers increases, κ decreases as a result of the inter-layer scattering effect.[3,63] The κ of suspended and supported 1 to 3-layered graphene is presented in the figure to

help readers have a better understanding of the level and range of our thermal conductivity. The boundary scattering due to the abundant pore structure and small flake size limits the overall in-plane κ of our GP. The κ of GP should be lower than that of the single-layered or few layered graphene due to the structure phonon scattering.

The thermal strain caused by a temperature decrease results in the mismatch and separation among the neighboring graphene flakes, which is responsible for the κ jump. Since the GP is composed of high purity graphene with very little impurities, the in-plane phonon scattering mean relaxing time is very long. The phonon propagation in GP is largely impacted by substrate scattering from neighboring impurity-embedded flakes. From Raman analysis of the structure, it is seen that the backbone of GP is 5–6-layered graphene flakes. Literature reports suggested that the top oxide deposition penetrates a characteristic distance of approximately 7 layers into the core layers of graphene at RT.[57] The impact of the substrate on the thermal transport in few-layered graphene is weaker with the increase of the layer thickness.[64] Wang *et al.* reported that when the supported 3-layered graphene length is 5.0 μm, the κ at RT is 1250 W m^{-1} K^{-1}.[58] This value is one fold lower than the reported 2300 W m^{-1} K^{-1} for suspended 3-layered graphene of 5 μm width.[3] For our GP, the separation and switch-on results in a 3.13–6.95 times higher κ. The discrepancy could result from the much smaller planar size of the graphene flakes (≤1.6 μm) in GP than that of graphene in the literature (L = 5 μm). Wang *et al.* found out that the substrate effect is more significant for smaller graphene sizes.[58] Besides, the substrate effect for GP is from both sides of graphene flakes rather than from one side only, which amplifies the suppression effect on thermal transport. Jang *et al.*[57] investigated the impact of the upper oxide deposition on a supported few layered graphene. An extra 38% reduction in κ at RT was observed for 4-layered graphene. In addition, the atomic mass and the type of atom of the substrate also play important roles in affecting the thermal transport in graphene. The coupling strength of graphene is expected to be stronger with carbon atoms in the substrate than other lighter or heavier atoms.[44] Although it is stacked into a good layered structure by mechanical compression, there are inter-flake spaces and openings inside GP. GP's density (1623 kg m^{-3}) is measured to be lower than that of graphite (2200 kg m^{-3}). Therefore, GP is not actually a material with full density. If we remove the inter-flake space and calculate the κ of GP in full density, the κ value could be higher. The κ at full density could reach 2348–4084 W m^{-1} K^{-1} after switching-on and 859–962 W m^{-1} K^{-1} before switching-on. These values are still reasonable on comparing with the reported value of suspended and supported graphene respectively.

The thermal contact resistance among the graphene flakes along the thickness direction and thermal strain in a single flake could affect the thermal transport in GP, but the overall switch-on behavior of κ is not influenced by these effects. Kuang *et al.*'s work demonstrated that the thermal strain in pure graphene flakes may enhance the thermal transport.[11] To estimate the applied strain on the thermal properties of graphene due to TEC mismatch, the previous experimental TEC value of -7×10^{-6} K^{-1} can be used.[65] If we assume that the temperature changes from 300 K to 0 K, the resulting thermal expansion is 0.0021, which is very small. According to the result reported in Kuang *et al.*'s work,[11] a thermal strain of 0.0021 results in less than 1.4% of κ variation for 3-layered graphene, which is almost negligible. It is indicated in Huang *et al.*'s work that the specific heat of the GP could be affected by the thermal strain. However, the thermal strain in GP is very small in the whole low temperature range in our work. If 0.0021 is used for the upper bound of strain, the corresponding specific heat variation is less than 0.7%. The main features of the result, including the resulting κ jump, are not affected. The thermal contact resistance in the thickness direction is expected to be very small. GP is composed of graphene flakes stacking together by the VdW force. From the XRD result, GP has an interlayer spacing of 3.35 Å which is the same as that of pyrolytic graphite. From the literature, κ in the direction perpendicular to the layer plane of graphite is reported to be 5.7 W m^{-1} K^{-1}.[62] The contacting and overlapping areas among the neighboring flakes are large. To transfer heat from one end to the other, there are multiple routes in the GP sample. Even for one single flake, there can be several flakes interconnecting with it, which reduces the thermal contact resistance effect significantly.

5. A comparison study against graphene oxide and partly reduced graphene paper

5.1 Thermal conductivity comparison

For the observed κ switch-on, one indispensable condition is that there are both pure graphene flakes and impurity-embedded flakes in the sample. These flakes have a different thermal expansion coefficient from the pure graphene flakes. However, graphene-related papers with impurities could not always facilitate structure separation and an ultra-high κ switch-on. In this section, the κ variation against temperature for graphene oxide paper (GOP) and partly reduced graphene paper (PRGP) is studied for comparison. PRGP and GOP are purchased from Advanced Chemical Supplier (ASC) Material and used as received.

Fig. 5(a) and (b) show the measured κ of PRGP and GOP respectively. The steady-state electro-thermal (SET)[37,66] technique is used for measuring the thermal conductivity. The details of the three PRGP samples and one GOP sample are presented in Table 1. The κ of PRGP ranges from 0.14 W m^{-1} K^{-1} at 15 K to 9.31 W m^{-1} K^{-1} at 300 K. As the temperature goes down, the κ of all of the four groups decreases in a similar trend. The κ values of the three PRGP samples are much smaller than that of GP, taking only about 1.2% of the κ of GP at RT. No switch-on behavior is observed for the κ of PRGP. The κ of GOP is presented in Fig. 5(b). As the tempera-

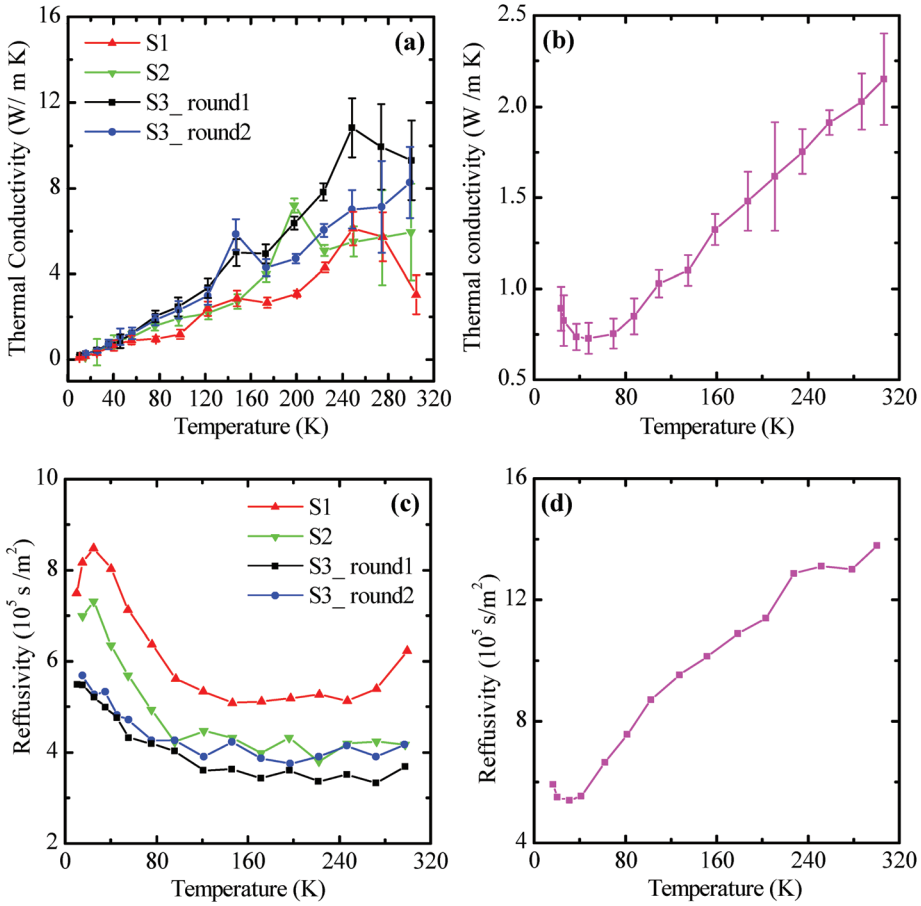

Fig. 5 The thermal conductivity of (a) PRGP and (b) GOP. The thermal reffusivity of (c) PRGP and (d) GOP. The measurement uncertainty is about ±10%. The error bar is omitted for purposes of clarity.

ture goes down, the κ of GOP decreases from 2.15 W m^{-1} K^{-1} at 306 K to 0.73 W m^{-1} K^{-1} at 37 K. At about 69 K, the κ becomes stable with a small increase at 25–23 K. The κ evolution of GOP constitutes a continuous curve with no switch-on behavior.

5.2 Thermal reffusivity and in-plane domain size

To interpret the different structures of PRGP and GOP, the thermal reffusivity of the two materials is measured using TET. Unlike GP, the TET signal for PRGP presents pure voltage decreasing patterns for the whole temperature range from 300 K to 10 K, which is also the case for previously reported graphene foam and graphene aerogel materials.[30,37] No dual thermal transport modes are observed. For the electrically non-conductive GOP, the TET signal is pure voltage increasing, which is from the Ir coating. Fig. 5(c) and (d) present the thermal reffusivity profiles of PRGP and GOP respectively. As mentioned above, the error for measurement is about ±10% in TET. The error bar is omitted for clarity. The Θ of GOP shows a similar behavior as that of GP. As the temperature goes down, Θ slowly reaches the residual Θ at about 5.5×10^5 s m^{-2}. By the thermal reffusivity model fitting, the Debye temperature and Θ_0 are determined to be 321 ± 23 K and $(5.54 \pm 0.16) \times 10^5$ s m^{-2} respectively. Accordingly, the structure domain size is calculated to be 5.9 Å, which is extremely small compared to that of GP (1.68 μm). This result indicates the dense impurities of GOP. The Θ profile of PRGP is very different from that of GP. At relatively high temperatures from 300 K to 121 K, four groups of Θ fluctuate within very narrow limits. Below 121 K, Θ starts to increase rapidly. The Θ of S1 increases from 5.5×10^5 s m^{-2} to 8.5×10^5 s m^{-2} at 25 K, then it drops a little from 25 K to 10 K. The Θ of S2 rises from 4.2×10^5 s m^{-2} to 7.3×10^5 s m^{-2} at 25 K. For S3, a repeated experiment is conducted when the temperature is elevated from 10 K back to 300 K. The resulting data of the first round and the second round are consistent. The Θ of S3 changes from around 4×10^5 s m^{-2} at 121 K to 5.5×10^5 s m^{-2} at 15 K.

5.3 Structure study and physics interpretation

The κ and Θ evolution of PRGP and GOP are attributed to the structure of the materials. Fig. 6 shows the structure characterization of the two materials, in anticipation to help interpret the observations in Fig. 5. Fig. 6(a) and (b) are the SEM images of PRGP and GOP respectively. Unlike the smooth and uniform surface of the GP, extensive ridges and wrinkles are observed at the surface of PRGP and GOP. For GOP, more

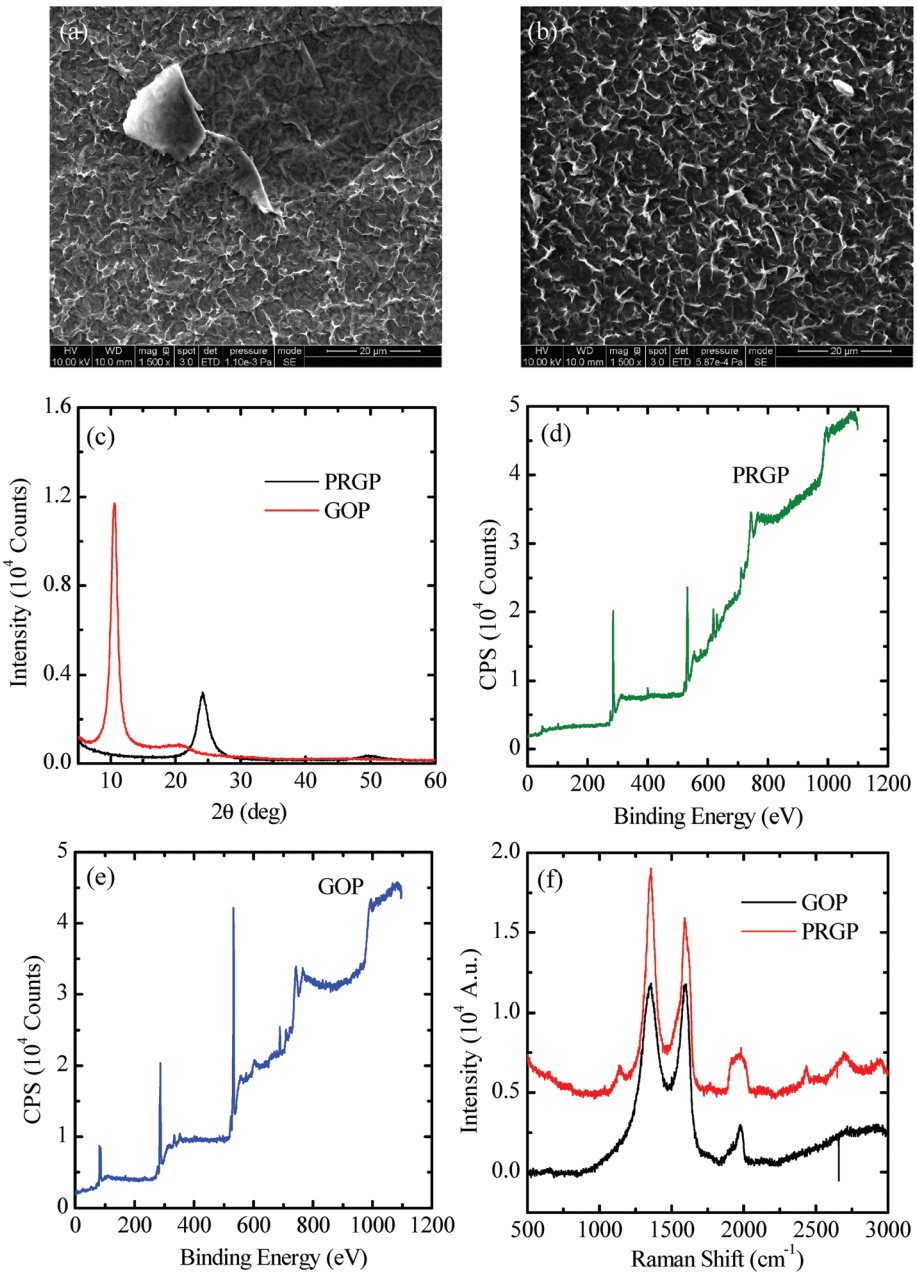

Fig. 6 SEM images of (a) PRGP and (b) GOP. (c) XRD spectra of PRGP and GOP. XPS survey spectra of (d) PRGP and (e) GOP. (f) The Raman spectra of PRGP and GOP, indicating the presence of defects and impurities in the samples.

impurities are present under the SEM. Fig. 6(c) shows the XRD results of PRGP and GOP. The XRD pattern for PRGP presents a major peak at around 24.15°, yielding an interlayer spacing of 3.68 Å. For comparison, the interlayer spacing of GP and graphite is about 3.35 Å.[33] The larger interlayer spacing of PRGP demonstrates the presence of residual oxygen and functional groups in PRGP. The major peak for GOP is at 10.52°. The interlayer spacing is 8.40 Å, which is consistent with the literature value of 8.32 Å at 10.6° for graphene oxide.[67] Compared with the narrow and distinct peak of GP, the XRD peaks of PRGP and GOP are relatively wider with a lower intensity, revealing that the crystalline structure is not as good as that of GP. PRGP presents an even wider peak with a lower intensity than that of GOP. Fig. 6(d) and (e) show the XPS survey spectra of PRGP and GOP. The result indicates the existence of other chemical bonds such as O 1s (25.1%), N 1s (2.50%), Fe 2p (1.98%) and I 3d (1.51%) on the surface of PRGP. For GOP, the chemical bond composition is C 1s (61.76%), O 1s (34.40), Au 4f (1.13%), F 1s (1.63%) and Fe 2p (1.07%). Fig. 6(f) shows the Raman spectra of PRGP and GOP. Two pronounced peaks at around 1354 cm^{-1} for the D peak and at 1593 cm^{-1} for the G peak are observed for PRGP. The GOP exhibits a D peak at around 1352 cm^{-1} and a G peak at around 1588 cm^{-1}. The 2D peak for GOP is almost invisible,

and is very small for PRGP. The D peak intensities are very high for both PRGP and GOP, indicating the large amount of defects and impurities in the materials. The I_D/I_G ratio for PRGP is higher than that of GOP, indicating that the reduction process results in in-plane C=C bond cracks. A large number of disorders are induced in the sp^2 domains. This is a commonly reported phenomenon for partly reduced graphene materials.[37,68,69] With further reduction, the I_D/I_G ratio could go down again due to the restoring of the sp^2 domains.[70] For comparison, the D peak for GP is invisible, which implies the high quality crystals in GP.

For GOP, the thermal reffusivity pattern reflects the dominant role of N-scattering at near RT and the impurity and defect phonon scattering at low temperatures, which is similar to that of GP. From the above characterization, there are a large amount of defects and other impurity atoms on GOP. This is in accordance with the high Θ_0 value of GOP. For PRGP, since parts of the oxygen groups have been removed by reduction, the newly emerged graphene domains in the sample make the PRGP electrically conductive (conductivity $\sim 5 \times 10^3$ S m^{-1}). For comparison, the electrical conductivity of GP is about 4.4×10^4 S m^{-1}, which is about one order of magnitude higher than that of PRGP. The κ of GP ($\sim$634 W m^{-1} K^{-1}) is about 68 times higher than that of PRGP (9.31 W m^{-1} K^{-1}) at RT. The large discrepancy is mainly attributed to the oxygen content and the functional groups on the surface of PRGP. The κ and Θ profiles of PRGP are very similar to that of the graphene aerogel (GA) which we studied and reported before.[37] The main mechanism controlling the thermal transport is the thermal contact resistance at interfaces. When the thermal contact resistance is very large, the effective κ of the sample can be deduced as $\Theta_{eff} = A/\nu l_f$.[37] In this expression, A is a correlation constant; ν is the phonon velocity and l_f is the average flake size of PRGP, which are both insensitive to the temperature change. This is the reason that the Θ of PRGP fluctuates within a very narrow limit from 300 K to 121 K. Under 121 K, the thermal expansion among the partly reduced graphene flakes deteriorates the contact among r-GO sheets and contributes to the increased thermal reffusivity.[37]

The reason why only GP presents the switching-on behavior can be summarized as follows. There might be structure separation in PRGP and GOP as well, but the separation has an insignificant effect on thermal transport. The phonon propagation in PRGP and GOP is largely suppressed by the in-plane impurity scattering and the interface scattering at the flake boundary. For GOP, the highly dense oxygen content and impurities lead to the dominating role of impurity scattering in thermal transport. Besides, the much larger interlayer spacing inhibits the neighboring impurity layer scattering effect to a great extent. For PRGP, although part of the oxygen content has been removed during the reduction process, the residual functional groups on the surface of PRGP flakes result in a weaker inter-flake bonding. The interface thermal contact resistance dominates the thermal transport in PRGP. As a result, the expansion induced separation and the neighboring impurity layer scattering change make a relatively insignificant contribution compared to the in-plane scattering and the interface scattering. Therefore, no switch-on behavior can be observed for κ and the diffusivity of PRGP and GOP. On the other hand, the pure graphene flakes in GP have a very low impurity density. The intensities of impurity scattering and interface scattering are extremely low. The neighboring flake scattering effect dominates over the point defect scattering and the thermal contact resistance in thermal transport. As a result, the switch-on effect is evidently observable from α and κ of GP. The difference in the thermal expansion between pure graphene flakes and impurity-embedded flakes plays the most important role in the switch-on in GP.

The thermal diffusivity data in this work are collected using the transient electro-thermal (TET) technique. In this technique, we only need a few parameters: the length of the sample and the voltage against time data. The length of the sample is measured using INFINITY ANALYZE software under a microscope with high accuracy and repeatability. A stage micrometer is used for calibration before the measurement. The resolution of the length measurement with INFINITY ANALYZE can be 0.01 μm. We measured the length of the sample 5 times and calculated the standard deviation. The voltage evolution is measured using an oscilloscope. Four-probe I–V measurement is employed in the experiment to reduce the effect of contact resistance. The collected data are then fitted with our physical model. For each thermal diffusivity measurement, we conducted 30 measurements and fittings. The deviation in $\alpha_{measure}$ is calculated. For the temperature measurement, we used DT-400 Series Silicon Diodes to monitor the temperature of the base on which the sample is suspended. The accuracy of the temperature measurement is ±0.5 K when the temperature is lower than 30 K, and ±0.25 K for 30–60 K, and ±0.15 K for 60–345 K. Combining the measurement uncertainty and the data variation mentioned above, the error of the measured thermal diffusivity is around ±10%.

The thermal conductivity of GP is calculated from the data of the measured thermal diffusivity and the specific heat of graphite. We only presented the error from the experimentally measured thermal diffusivity and error of the density of the GP sample, while the error of the specific heat is neglected. The error of the density is presented in Table 1. The specific heat data of pyrolytic graphite are from the experimental data in the literature. The measurement error is very small ($\leq$5%). The discrepancy of specific heat between GP and graphite is mainly from the different interlayer coupling strengths and lattice strains from temperature. Although there are no experimental data about the level of deviation, the specific heat of GP is expected to be close to that of graphite since the GP consists of 5–6-layered graphene. The specific heat error could cause all the thermal conductivities below 100 K to move to a higher level, but the switch-on pattern of GP at around 200 K is not affected. The thermal conductivities of PRGP and GOP are obtained using the steady-state electro-thermal (SET) technique. The error of the measurement is larger than the thermal diffusivity data since this technique requires the

knowledge of the thickness, width of the sample and the temperature coefficient of resistance. In this method, the κ at each temperature is obtained by: $\kappa_m = I^2R_1L(dR/dT)/12A_c\Delta R$. The error of κ_m is calculated following the error propagation rule.

The measurement error of thermal conductivity in our experiment is smaller than that of mono-layered and multi-layered graphene reported in other literature studies. GP is a bulk material with a much larger sample size. Some literature reports determined the thermal conductivity of graphene from the heat transfer model at the steady state, such as the thermal bridge method.[6] The measurement error is mainly from the thermal contact resistance between the thin graphene sample and the electrodes underneath graphene. For comparison, we use a silver paste to connect the bulk GP sample with the gold-coated silicon electrodes. The particle size in the silver paste is much smaller than that of the GP sample. We also use the four-probe method to obtain the voltage data, which significantly reduce the effect of electrical contact resistance. In our previous work, the thermal diffusivity of silver paste connected Pt wires has been measured using TET. The resulting data agree well with the reference value, which indicates that the thermal contact resistance is negligible.[71] The measured GP sample is very long (~1.7 cm), which means that the intrinsic thermal resistance of GP is much larger than that of the thermal contact resistance. The contacting area with electrodes is much larger as well. The thermal contact resistance takes less than 6% of the thermal resistance if calculated from Fujishiro *et al.*'s experimental report. The thermal contact resistivity between a high-T_c superconductor and a copper block connected by silver paste is quite stable at around 100 mm^2 K W^{-1} from 40 K to 200 K.[72] The contacting area between GP and the silver paste is around 0.2 mm × 1 mm × 4 in our experiment. The thermal contact resistance at two ends of the sample can be estimated to be 125 K W^{-1}. For comparison, the thermal resistance of the GP sample is about 2117 K W^{-1} at 195 K. Other indirect methods of thermal characterization reported larger measurement errors. The measurement error of thermal conductivity from the Raman thermometry measurement is known to be quite large.[7] To obtain the final thermal conductivity data, they need to do the Raman peak position calibration first. The data scattering was mainly attributed to the variation in the optical absorption from membrane to membrane and the large uncertainty of the measurement of temperature with the Raman spectrometer.

From the experimental aspect, it is still very challenging to directly observe the separation of graphene flakes in the thickness direction. To this end, it would be constructive to describe how to probe the electrical and thermal conductivity change due to the temperature induced structure change. However, the experiment is challenging and needs a delicate design. GP has a very small thickness (28.6 μm) and large in-plane size, therefore the electrical resistance along the thickness direction will be extremely small. The structure separation is in the thickness direction and the structure change due to temperature variation is very small. The probes of potential experiments need to be controlled in such a way that the contact resistance is negligible and independent of the temperature while the structure separation can happen without external constraint. We will design the sample setup in the cryogenic station and use principles similar to the laser flash experiment for thickness-direction thermal characterization. The electrical and thermal properties of GP in the thickness direction will be studied in detail in the near future.

6. Conclusion

A novel high thermal conductivity/diffusivity switch-on behavior was discovered for high purity GP when its temperature was reduced to 245–260 K. Upon switch-on, the thermal diffusivity and thermal conductivity of GP had a 4 to 8-fold jump. The ultra-high thermal conductivity switch-on was also observed to be reversible during a single TET heating process. It suggests that the thermal expansion coefficient difference between pure graphene flakes and the surrounding impurity flakes causes separation of the flakes at certain temperatures. When GP flakes are in the contacting state, the interaction between pure graphene flakes and surrounding impurity-embedded flakes efficiently suppresses phonon transport in GP. After switching-on, the flakes are free from the substrate scattering effect. The physics explanation was also confirmed by the TCR switch behavior during the TET measurement. By conducting repeated experiments, the structure separation was found to be repeatable. When the temperature goes back to RT, the flakes go back to the original contacting state. The measured κ values of before and after switch-on were consistent with the literature reported κ values of supported and suspended graphene respectively. The thermal conductivity and thermal reffusivity profiles of graphite, PRGP and GOP were presented and compared to analyze the requirements for the switch-on. No switch-on behavior was observed for PRGP and GOP. The extremely low intensity of the point defect scattering and the small thermal contact resistance in GP result in the strong influence of the neighboring impurity layer scattering in GP. This makes the thermal expansion induced switch-on feasible. This finding points out a novel way to switch on/off the ultra-high thermal conductivity of graphene paper based on substrate–phonon scattering.

7. Experimental details

The SEM images are taken by using an FEI Quanta 250 field emission SEM with a voltage of 10.00 kV. The Raman spectrum is acquired under a 50× lens (Olympus BX51 universal research Microscopy) by 532 nm laser excitation with a power of 8.899 mW and an integration time of 12 s. The X-ray diffraction (XRD) is conducted with a Siemens D500 X-ray diffractometer using a Cu X-ray tube operated at 30 kV and 5 mA. The XPS measurement is performed using a Kratos Amicus/ESCA 3400 instrument irradiated with 240 W unmonochromated Mg Kα X-rays. The pass energy is set at 75 eV and the Shirley base-

line is removed from all reported spectra. CasaXPS is used to process raw data files.

The thermal diffusivities of GP samples at different temperatures are measured using the transient electro-thermal (TET) technique. A Janis closed cycle refrigerator (CCR) system is utilized to provide stable environmental temperatures from 295 K to 10 K. To avoid the effect of contact resistance at both sides of the sample connection, four-probe *I–V* measurement is employed in the experiment. Fig. 2(a) shows the schematic of the experimental set up, which shows the suspended sample placed on the stage of the cold head of the CCR system. Two samples are measured. The details of the two samples are summarized in Table 1. Three rounds of experiments are conducted, denoted as S1_round1, S1_round2 and S2 respectively. The GP sample is suspended between two gold coated silicon electrodes on a thin glass wafer. A small amount of silver paste is used for attaching four wires to the electrodes of the GP. A current source provides a step current flowing through the sample. The voltage evolution is measured using an oscilloscope. The step current induces a joule heating in the sample. The temperature of the GP sample first increases and then becomes stable through heat conduction and thermal radiation. In the vacuum jacket, where a high vacuum environment (air pressure lower than 0.5 mTorr) is maintained, heat convection though air is negligible. The normalized average temperature rises, which is defined as $T^* = [T(t) - T_0]/[T_\infty - T_0]$, and is given as:

$$T^* = \frac{48}{\pi^4}\sum_{m=1}^{\infty}\frac{1-(-1)^m}{m^2}\frac{1-\exp[-m^2\pi^2\alpha_m t/L^2]}{m^2}, \qquad (1)$$

where L is the suspended length of the sample; t is the time; and α_m is the measured thermal diffusivity. The temperature increase is controlled to be much smaller than the environmental temperature ($\Delta T \ll T_0$). In the small temperature range, a linear relationship between the resistance and the sample temperature can be used. By measuring the voltage evolution, the resistance profile is determined, and subsequently the normalized temperature rise is obtained. Using Matlab programming, different trial values of α_m are used to fit the normalized temperature curve. The α_m value giving the best fitting is determined as the measured thermal diffusivity of the sample. More details about the TET physical principle and experimental set up can be found in our previous work.[31,40,73–75]

The measured thermal diffusivity is a combination of the intrinsic thermal diffusivity (α) and the heat radiation effect: $\alpha_{measure} = \alpha + 8\varepsilon_r\sigma\bar{T}^3L^2/\rho c_p\pi^2 D$. In this equation, the first term α is the real thermal diffusivity of the GP sample; the second term is the radiation effect. ρc_p is the volumetric specific heat; ε_r is the emissivity; σ is the Stefan–Boltzmann constant; $\bar{T}$ is the average temperature of the sample during the heating process; and D is the thickness of the sample. The thicknesses of the two samples (S1 and S2) are considered the same since they are cut from a GP film with a uniform thickness. To estimate the radiation effect, the longer sample S2 at 300 K is studied. Using the length of S2 of 18.5 mm, thickness of 28.6 μm, emissivity of 1 (upper limit), and the specific heat of graphite at 710 J kg^{-1} K^{-1}, the radiation part of thermal diffusivity is estimated to be 1.29×10^{-5} m^2 s^{-1}. Since the measured thermal diffusivity of GP is about 6.2×10^{-4} m^2 s^{-1} at RT, the radiation effect only takes about 2% of the measured thermal diffusivity at 300 K for S2. At lower temperatures, the radiation effect decreases by T^3. For S1_round1 and S1_round2, the radiation effect is lower than S2 due to the shorter sample lengths. Therefore, the radiation effect takes less than 2% of the measured thermal diffusivity of the three experiments. It is neglected for the GP samples from 300 K to 10 K.

The steady-state electro-thermal (SET) technique is used for measuring the κ of PRGP and GOP. The experimental set-up is the same as that of TET. The difference is that the SET technique utilizes the data before the joule heating and at the steady state of the joule heating. In this method, the κ at each temperature is obtained by: $\kappa_m = I^2R_1L(dR/dT)/12A_c\Delta R$. In the equation, κ_m is the measured thermal conductivity, I is the current flowing through the sample, R_1 is the resistance of the sample at the steady state, dR/dT is obtained by differentiating the R_0–T curve, A_c is the cross-section area of the sample, and ΔR is the resistance change induced by the joule heating. Considering that GOP is electrically nonconductive, a thin layer of the Ir film (20 nm) is sputter coated on the top surface of the GOP. The coating effect and the radiation effect are evaluated and subtracted as $\kappa_{real} = \kappa_m - 8\varepsilon_r\sigma T^3L^2/\pi^2 D - L_{Lorenz}TL/R_1A_c$. In the equation, the second term on the right is the radiation effect, in which ε_r is the emissivity, σ the Stefan–Boltzmann constant, and D the thickness of the sample. The third term on the right is the coating effect, in which L_{Lorenz} is the Lorenz number for Ir. The equation has been deduced and used in our previous studies.[30,31,76] The resulting radiation effect and the coating effect are very small compared to that of the measured κ, taking less than 2% of κ_m. Therefore, the error from subtracting the radiation effect and the coating effect is insignificant on the final result. This method is not used for the κ measurement of GP because the R–T curve of GP is complicated and could bring in large errors in dR/dT calculation.

Acknowledgements

Support of this work by the Iowa Energy Center (OG-15-011), the National Science Foundation (CBET1235852, CMMI1264399) and the Department of Energy (DENE0000671) is gratefully acknowledged. Y. Xie is grateful to the China Scholarship Council for their great support. X. W. acknowledges the partial support of the "Taishan Scholar" Program of Shandong, China.

References

1 A. A. Balandin, S. Ghosh, W. Z. Bao, I. Calizo, D. Teweldebrhan, F. Miao and C. N. Lau, *Nano Lett.*, 2008, **8**, 902–907.

2 S. Ghosh, I. Calizo, D. Teweldebrhan, E. P. Pokatilov, D. L. Nika, A. A. Balandin, W. Bao, F. Miao and C. N. Lau, *Appl. Phys. Lett.*, 2008, **92**, 15–17.
3 S. Ghosh, W. Z. Bao, D. L. Nika, S. Subrina, E. P. Pokatilov, C. N. Lau and A. A. Balandin, *Nat. Mater.*, 2010, **9**, 555–558.
4 W. W. Cai, A. L. Moore, Y. W. Zhu, X. S. Li, S. S. Chen, L. Shi and R. S. Ruoff, *Nano Lett.*, 2010, **10**, 1645–1651.
5 L. A. Jauregui, Y. N. Yue, A. N. Sidorov, J. N. Hu, Q. K. Yu, G. Lopez, R. Jalilian, D. K. Benjamin, D. A. Delk, W. Wu, Z. H. Liu, X. W. Wang, Z. G. Jiang, X. L. Ruan, J. M. Bao, S. S. Pei and Y. P. Chen, *ECS Trans.*, 2010, **28**, 73–83.
6 X. Xu, L. F. C. Pereira, Y. Wang, J. Wu, K. W. Zhang, X. M. Zhao, S. Bae, C. T. Bui, R. G. Xie, J. T. L. Thong, B. H. Hong, K. P. Loh, D. Donadio, B. W. Li and B. Ozyilmaz, *Nat. Commun.*, 2014, **5**, 3689.
7 S. S. Chen, Q. Z. Wu, C. Mishra, J. Y. Kang, H. J. Zhang, K. J. Cho, W. W. Cai, A. A. Balandin and R. S. Ruoff, *Nat. Mater.*, 2012, **11**, 203–207.
8 J. H. Seol, I. Jo, A. L. Moore, L. Lindsay, Z. H. Aitken, M. T. Pettes, X. S. Li, Z. Yao, R. Huang, D. Broido, N. Mingo, R. S. Ruoff and L. Shi, *Science*, 2010, **328**, 213–216.
9 W. Jang, Z. Chen, W. Bao, C. N. Lau and C. Dames, *Nano Lett.*, 2011, **11**, 3049–3049.
10 M. T. Pettes, I. S. Jo, Z. Yao and L. Shi, *Nano Lett.*, 2011, **11**, 1195–1200.
11 Y. D. Kuang, L. Lindsay and B. L. Huang, *Nano Lett.*, 2015, **15**, 6121–6127.
12 D. Yoon, Y. W. Son and H. Cheong, *Nano Lett.*, 2011, **11**, 3227–3231.
13 G. H. Li, A. Luican and E. Y. Andrei, *Phys. Rev. Lett.*, 2009, **102**, 176804.
14 N. J. Song, C. M. Chen, C. X. Lu, Z. Liu, Q. Q. Kong and R. Cai, *J. Mater. Chem. A*, 2014, **2**, 16563–16568.
15 G. Q. Xin, H. T. Sun, T. Hu, H. R. Fard, X. Sun, N. Koratkar, T. Borca-Tasciuc and J. Lian, *Adv. Mater.*, 2014, **26**, 4521–4526.
16 F. Liu, S. Y. Song, D. F. Xue and H. J. Zhang, *Adv. Mater.*, 2012, **24**, 1089–1094.
17 H. Wu and L. T. Drzal, *Carbon*, 2012, **50**, 1135–1145.
18 J. K. Lee, K. B. Smith, C. M. Hayner and H. H. Kung, *Chem. Commun.*, 2010, **46**, 2025–2027.
19 A. Abouimrane, O. C. Compton, K. Amine and S. T. Nguyen, *J. Phys. Chem. C*, 2010, **114**, 12800–12804.
20 C. Y. Wang, D. Li, C. O. Too and G. G. Wallace, *Chem. Mater.*, 2009, **21**, 2604–2606.
21 H. Gwon, H. S. Kim, K. U. Lee, D. H. Seo, Y. C. Park, Y. S. Lee, B. T. Ahn and K. Kang, *Energy Environ. Sci.*, 2011, **4**, 1277–1283.
22 S. S. Li, Y. H. Luo, W. Lv, W. J. Yu, S. D. Wu, P. X. Hou, Q. H. Yang, Q. B. Meng, C. Liu and H. M. Cheng, *Adv. Energy Mater.*, 2011, **1**, 486–490.
23 O. C. Compton, D. A. Dikin, K. W. Putz, L. C. Brinson and S. T. Nguyen, *Adv. Mater.*, 2010, **22**, 892–896.
24 C. Valles, J. D. Nunez, A. M. Benito and W. K. Maser, *Carbon*, 2012, **50**, 835–844.
25 W. B. Hu, C. Peng, W. J. Luo, M. Lv, X. M. Li, D. Li, Q. Huang and C. H. Fan, *ACS Nano*, 2010, **4**, 4317–4323.
26 J. L. Xiang and L. T. Drzal, *Carbon*, 2011, **49**, 773–778.
27 V. K. Tewary and B. Yang, *Phys. Rev. B: Condens. Matter*, 2009, **79**, 125416.
28 Z. L. Xu, S. Xu, X. D. Tang and X. W. Wang, *AIP Adv.*, 2014, **4**, 017131.
29 Z. Cheng, Z. L. Xu, S. Xu and X. W. Wang, *J. Appl. Phys.*, 2015, **117**, 024307.
30 Y. S. Xie, Z. L. Xu, S. Xu, Z. Cheng, N. Hashemi, C. Deng and X. W. Wang, *Nanoscale*, 2015, **7**, 10101–10110.
31 J. Liu, Z. L. Xu, Z. Cheng, S. Xu and X. W. Wang, *ACS Appl. Mater. Interfaces*, 2015, **7**, 27279–27288.
32 D. Graf, F. Molitor, K. Ensslin, C. Stampfer, A. Jungen, C. Hierold and L. Wirtz, *Nano Lett.*, 2007, **7**, 238–242.
33 T. A. Pham, J. Kim, J. S. Kim and Y. T. Jeong, *Colloids Surf., A*, 2011, **386**, 195–195.
34 C. M. Kassis, J. K. Steehler, D. E. Betts, Z. B. Guan, T. J. Romack, J. M. DeSimone and R. W. Linton, *Macromolecules*, 1996, **29**, 3247–3254.
35 C. Hontorialucas, A. J. Lopezpeinado, J. D. D. Lopezgonzalez, M. L. Rojascervantes and R. M. Martinaranda, *Carbon*, 1995, **33**, 1585–1592.
36 C. M. Chen, J. Q. Huang, Q. Zhang, W. Z. Gong, Q. H. Yang, M. Z. Wang and Y. G. Yang, *Carbon*, 2012, **50**, 659–667.
37 Y. S. Xie, S. Xu, Z. L. Xu, H. C. Wu, C. Deng and X. W. Wang, *Carbon*, 2016, **98**, 381–390.
38 J. Q. Guo, X. W. Wang, L. J. Zhang and T. Wang, *Appl. Phys. A: Mater. Sci. Process.*, 2007, **89**, 153–156.
39 X. H. Feng, X. P. Huang and X. W. Wang, *Rev. Sci. Instrum.*, 2012, **83**, 044901.
40 H. Lin, S. Xu, X. W. Wang and N. Mei, *Nanotechnology*, 2013, **24**, 415706.
41 L. F. Huang and Z. Zeng, *J. Appl. Phys.*, 2013, **113**, 083524.
42 Z. X. Guo, D. Zhang and X. G. Gong, *Appl. Phys. Lett.*, 2009, **95**, 163103.
43 X. B. Li, K. Maute, M. L. Dunn and R. G. Yang, *Phys. Rev. B: Condens. Matter*, 2010, **81**, 245318.
44 J. Liu, T. Wang, S. Xu, P. Yuan, X. Xu and X. Wang, *Nanoscale*, 2016, **8**, 10298–10309.
45 H. Pang, Y. C. Zhang, T. Chen, B. Q. Zeng and Z. M. Li, *Appl. Phys. Lett.*, 2010, **96**, 251907.
46 L. Lindsay, D. A. Broido and N. Mingo, *Phys. Rev. B: Condens. Matter*, 2010, **82**, 115427.
47 A. S. Nissimagoudar and N. S. Sankeshwar, *Phys. Rev. B: Condens. Matter*, 2014, **89**, 235422.
48 L. A. Falkovsky, *Phys. Rev. B: Condens. Matter*, 2007, **75**, 153410.
49 F. Liu, P. M. Ming and J. Li, *Phys. Rev. B: Condens. Matter*, 2007, **76**, 064120.
50 J. C. Zhang, X. P. Huang, Y. N. Yue, J. M. Wang and X. W. Wang, *Phys. Rev. B: Condens. Matter*, 2011, **84**, 235416.
51 K. Saito, J. Nakamura and A. Natori, *Phys. Rev. B: Condens. Matter*, 2007, **76**, 115409.

52 D. Singh, J. Y. Murthy and T. S. Fisher, *J. Appl. Phys.*, 2011, **110**, 044317.
53 Y. F. Chen, J. R. Lukes, D. Y. Li, J. K. Yang and Y. H. Wu, *J. Chem. Phys.*, 2004, **120**, 3841–3846.
54 E. Pop, V. Varshney and A. K. Roy, *MRS Bull.*, 2012, **37**, 1273–1281.
55 D. L. Nika, A. I. Cocemasov and A. A. Balandin, *Appl. Phys. Lett.*, 2014, **105**, 031904.
56 W. Desorbo and W. W. Tyler, *J. Chem. Phys.*, 1953, **21**, 1660–1663.
57 W. Y. Jang, Z. Chen, W. Z. Bao, C. N. Lau and C. Dames, *Nano Lett.*, 2010, **10**, 3909–3913.
58 Z. Q. Wang, R. G. Xie, C. T. Bui, D. Liu, X. X. Ni, B. W. Li and J. T. L. Thong, *Nano Lett.*, 2011, **11**, 113–118.
59 J. U. Lee, D. Yoon, H. Kim, S. W. Lee and H. Cheong, *Phys. Rev. B: Condens. Matter*, 2011, **83**, 081419.
60 G. A. Slack, *Phys. Rev.*, 1962, **127**, 694.
61 S. S. Chen, A. L. Moore, W. W. Cai, J. W. Suk, J. H. An, C. Mishra, C. Amos, C. W. Magnuson, J. Y. Kang, L. Shi and R. S. Ruoff, *ACS Nano*, 2011, **5**, 321–328.
62 C. Y. Ho, R. W. Powell and P. E. Liley, *J. Phys. Chem. Ref. Data*, 1972, **1**, 279–421.
63 W. R. Zhong, M. P. Zhang, B. Q. Ai and D. Q. Zheng, *Appl. Phys. Lett.*, 2011, **98**, 113107.
64 J. Chen, G. Zhang and B. W. Li, *Nanoscale*, 2013, **5**, 532–536.
65 W. Z. Bao, F. Miao, Z. Chen, H. Zhang, W. Y. Jang, C. Dames and C. N. Lau, *Nat. Nanotechnol.*, 2009, **4**, 562–566.
66 Z. Cheng, L. J. Liu, S. Xu, M. Lu and X. W. Wang, *Sci. Rep.*, 2015, **5**, 10718.
67 S. Park, J. An, J. R. Potts, A. Velamakanni, S. Murali and R. S. Ruoff, *Carbon*, 2011, **49**, 3019–3023.
68 H. Hu, Z. B. Zhao, W. B. Wan, Y. Gogotsi and J. S. Qiu, *Adv. Mater.*, 2013, **25**, 2219–2223.
69 S. Some, Y. Kim, Y. Yoon, H. Yoo, S. Lee, Y. Park and H. Lee, *Sci. Rep.*, 2013, **3**, 1929.
70 S. H. Huh, *Thermal reduction of graphene oxide*, InTech Open Access Publisher, 2011, pp. 73–90.
71 J. Q. Guo, X. W. Wang and T. Wang, *J. Appl. Phys.*, 2007, 101.
72 H. Fujishiro, T. Okamoto and K. Hirose, *Physica C*, 2001, **357**, 785–788.
73 J. Q. Guo, X. W. Wang and T. Wang, *J. Appl. Phys.*, 2007, **101**, 063537.
74 Z. Cheng, Z. Xu, L. Zhang and X. Wang, *PLoS One*, 2014, **9**, e114821.
75 H. Lin, S. Xu, Y. Q. Zhang and X. W. Wang, *ACS Appl. Mater. Interfaces*, 2014, **6**, 11341–11347.
76 G. Q. Liu, H. Lin, X. D. Tang, K. Bergler and X. W. Wang, *J. Visualized Exp.*, 2014, e51144.